TSUNAMI BENCHMARK RESULTS FOR NON-HYDROSTATIC WAVE MODEL NHWAVE VERSION 1.1

BY

BABAK TEHRANIRAD, JAMES T. KIRBY,

GANGFENG MA, FENGYAN SHI

RESEARCH REPORT NO. CACR-12-03
MAY 2012

CENTER FOR APPLIED COASTAL RESEARCH

Ocean Engineering Laboratory
University of Delaware
Newark, Delaware 19716

Abstract

This report describes tsunami benchmark testing of the non-hydrostatic wave model NHWAVE, carried out in conjunction with the National Tsunami Hazard Mitigation Program. The results presented here represent testing of Version 1.1 of the code, and will be updated online at http://chinacat.coastal.udel.edu/programs/nhwave.html with each version change for the publicly distributed code.

Contents

1 Model description **7**
1.1 Navier-Stokes equations 7
1.2 Governing equations in σ coordinate system 7

2 Numerical method **9**
2.1 Grid configuration 9
2.2 Time Stepping 10
2.3 Spatial finite volume scheme 11
2.4 Boundary conditions 14

3 Basic hydrodynamic considerations **15**
3.1 Mass conservation 15
3.2 Convergence 16

4 Analytical benchmark **16**
4.1 Solitary wave on a simple beach 16

5 Laboratory benchmarks **18**
5.1 Solitary wave on a simple beach 18
5.2 Solitary wave on a composite beach 21
5.3 Solitary wave on a conical island 22
5.4 3D underwater landslide 23

List of Figures

1 Layout of computational variables. Velocities (u, v, w) are placed at cell center and dynamic pressure p is defined at vertical cell face. 10
2 Definition sketch for simple beach bathymetry(from Synolakis et al (2007, Figure A1)). 17
3 Numerical simulation data for maximum runup of nonbreaking waves climbing up different beach slopes. Solid line represents the runup law (25). 18
4 The water level profiles during runup of the non-breaking wave in the case of $H/d = 0.019$ on a 1:19.85 beach. Solid blue line represents the analytical solution in according to Synolakis(1986), and dashed red lines represents the numerical simulation. 19
5 The water level dynamics at two locations $X/d = 0.25$ and $X/d = 9.95$. Solid blue line represents the analytical solution in according to Synolakis(1986), and dashed red line represents the numerical simulation. 20
6 Time evolution of nonbreaking $H/d = 0.0185$ initial wave. 21
7 Time evolution of breaking $H/d = 0.3$ initial wave. 22
8 Definition sketch for Revere Beach (from Synolakis et al (2007, Figure A7)). . . . 23
9 Time evolution of nonbreaking $H/d = 0.0378$ initial wave on composite beach. The red line shows the numerical solution and blue line represents the laboratory data. 24
10 Time evolution of breaking $H/d = 0.2578$ initial wave on composite beach. The red line shows the numerical solution and blue line represents the laboratory data. . 25
11 Time evolution of breaking $H/d = 0.6404$ initial wave on composite beach. The red line shows the numerical solution and blue line represents the laboratory data. . 26
12 View of conical island(top) and basin(bottom)(from Synolakis et al (2007, Figure A16)). 27
13 Definition sketch for conical island. All dimensions are in cm (from Synolakis et al (2007, Figure A17)). 27
14 Schematic gauge locations around the conical island(from Synolakis et al (2007, Figure A18)). 28
15 Comparison of computed and measured time series of free surface for $H/d = 0.045$. 29
16 Comparison of computed and measured time series of free surface for $H/d = 0.091$. 30
17 Comparison of computed and measured time series of free surface for $H/d = 0.181$. 30
18 Experimental setup of under water landslide experiments (Enet and Grilli, 2007) . . 31
19 Vertical Cross section of underwater landslide (Enet and Grilli, 2007) 32
20 Landslide Gauge Locations (Table 4) (Enet and Grilli, 2007) 33
21 Surface elevation of measured and computed data (Case A) 34
22 Surface elevation of measured and computed data (Case B) 35
23 Surface elevation of measured and computed data (Case C) 36
24 Surface elevation of measured and computed data (Case D) 37

25 Surface elevation of measured and computed data (Case E) 38
26 Surface elevation of measured and computed data (Case F) 39
27 Surface elevation of measured and computed data (Case G) 40

List of Tables

1 Maximum runup for gauge 9 for different grid size. 16
2 Runup data from numerical calculations compared with runup law values. 17
3 Measure and curve-fitted slide and wave parameters for various initial submergence depths (Enet and Grilli, 2007) 29
4 Wave Gauges Locations (Enet and Grilli, 2007) 32

1 Model description

NHWAVE is a fully nonlinear, non-hydrostatic, 3D solver for surface wave motion developed by Ma et al (2012). NHWAVE solves either the Euler equations or Reynolds-averaged Navier-Stokes equations in a time-dependent, surface- and bottom-following σ coordinate system. In Navier-Stokes applications, turbulent stresses are represented through use of a $k - \epsilon$ closure. In tsunami applications, the model is used to compute water column response to initial ground motion as well as near field propagation and runup. An overview of the model formulation and numerical implementation follows. Readers are referred to Ma et al (2012) for additional details of model development and testing.

In sections X and Y, the model is tested against standard NTHMP benchmarks obtained from Synolakis et al (2007) and Enet and Grilli (2007).

1.1 Navier-Stokes equations

The incompressible Navier-Stokes equations in Cartesian coordinates (x_1^*, x_2^*, x_3^*), where $x_1^* = x^*$, $x_2^* = y^*$ and $x_3^* = z^*$ and time t^* are given by

$$\frac{\partial u_i}{\partial x_i^*} = 0 \tag{1}$$

$$\frac{\partial u_i}{\partial t^*} + u_j \frac{\partial u_i}{\partial x_j^*} = -\frac{1}{\rho}\frac{\partial \tilde{p}}{\partial x_i^*} + g_i + \frac{\partial \tau_{ij}}{\partial x_j^*} \tag{2}$$

where $(i, j) = 1, 2, 3$, u_i is velocity component in the x_i^* direction, $\tilde{p}$ is total pressure, ρ is water density, $g_i = -g\delta_{i3}$ is the gravitational body force and $\tau_{ij} = \nu_t(\partial u_i/\partial x_j^* + \partial u_j/\partial x_i^*)$ is turbulent stress with ν_t the turbulent kinematic viscosity. Equations (1) and (2) are augmented by kinematic constraints given at the surface and bottom boundaries given by

$$\frac{\partial \eta}{\partial t^*} + u\frac{\partial \eta}{\partial x^*} + v\frac{\partial \eta}{\partial y^*} = w; \qquad z^* = \eta \tag{3}$$

$$\frac{\partial h}{\partial t^*} + u\frac{\partial h}{\partial x^*} + v\frac{\partial h}{\partial y^*} = -w; \qquad z^* = -h \tag{4}$$

where η and h are single valued functions of (x^*, y^*, t^*), and by appropriate dynamic constraints.

1.2 Governing equations in σ coordinate system

In order to accurately represent bottom and surface geometry, a σ coordinate transformation developed by Phillips (1957) is used in NHWAVE. The coordinate transformation maps the bottom and surface onto constant boundaries of a strip of unit thickness. The transformation is given by

$$t = t^* \quad x = x^* \quad y = y^* \quad \sigma = \frac{z^* + h}{D} \tag{5}$$

where $D = h + \eta$. Using the chain rule, the partial derivatives of a variable $f = f(x^*, y^*, z^*, t^*)$ in the physical domain are transformed as follows.

$$\begin{aligned}
\frac{\partial f}{\partial t^*} &= \frac{\partial f}{\partial t} + \frac{\partial f}{\partial \sigma}\frac{\partial \sigma}{\partial t^*} \\
\frac{\partial f}{\partial x^*} &= \frac{\partial f}{\partial x} + \frac{\partial f}{\partial \sigma}\frac{\partial \sigma}{\partial x^*} \\
\frac{\partial f}{\partial y^*} &= \frac{\partial f}{\partial y} + \frac{\partial f}{\partial \sigma}\frac{\partial \sigma}{\partial y^*} \\
\frac{\partial f}{\partial z^*} &= \frac{\partial f}{\partial \sigma}\frac{\partial \sigma}{\partial z^*}
\end{aligned} \tag{6}$$

We obtain the governing equations in the new coordinate system (x, y, σ, t) using (5-6) in (1) and (2). The continuity equation (1) is first transformed as

$$\frac{\partial u}{\partial x} + \frac{\partial u}{\partial \sigma}\frac{\partial \sigma}{\partial x^*} + \frac{\partial v}{\partial y} + \frac{\partial v}{\partial \sigma}\frac{\partial \sigma}{\partial y^*} + \frac{1}{D}\frac{\partial w}{\partial \sigma} = 0 \tag{7}$$

Using the results

$$\begin{aligned}
\frac{\partial \sigma}{\partial t^*} &= \frac{1}{D}\frac{\partial h}{\partial t} - \frac{\sigma}{D}\frac{\partial D}{\partial t} \\
\frac{\partial \sigma}{\partial x^*} &= \frac{1}{D}\frac{\partial h}{\partial x} - \frac{\sigma}{D}\frac{\partial D}{\partial x} \\
\frac{\partial \sigma}{\partial y^*} &= \frac{1}{D}\frac{\partial h}{\partial y} - \frac{\sigma}{D}\frac{\partial D}{\partial y} \\
\frac{\partial \sigma}{\partial z^*} &= \frac{1}{D}
\end{aligned} \tag{8}$$

we rewrite (7) as

$$\frac{\partial D}{\partial t} + \frac{\partial Du}{\partial x} + \frac{\partial Dv}{\partial y} + \frac{\partial \omega}{\partial \sigma} = 0 \tag{9}$$

where ω is the vertical velocity relative to constant σ surfaces, given by

$$\omega = D\left(\frac{\partial \sigma}{\partial t^*} + u\frac{\partial \sigma}{\partial x^*} + v\frac{\partial \sigma}{\partial y^*} + w\frac{\partial \sigma}{\partial z^*}\right) \tag{10}$$

The transformed continuity equation (9) may be integrated over depth to obtain

$$\frac{\partial D}{\partial t} + \frac{\partial}{\partial x}(D\int_0^1 u d\sigma) + \frac{\partial}{\partial y}(D\int_0^1 v d\sigma) = 0 \tag{11}$$

where the kinematic constraints (3) - (4) have been used. Equation (11) is used subsequently to determine the surface position.

The transformed momentum equations may be written as

$$\frac{\partial \mathbf{U}}{\partial t} + \frac{\partial \mathbf{F}}{\partial x} + \frac{\partial \mathbf{G}}{\partial y} + \frac{\partial \mathbf{H}}{\partial \sigma} = \mathbf{S}_h + \mathbf{S}_p + \mathbf{S}_\tau \tag{12}$$

where $\mathbf{U} = (Du, Dv, Dw)^T$. The fluxes are given by

$$\mathbf{F} = \begin{pmatrix} Duu + \frac{1}{2}gD^2 \\ Duv \\ Duw \end{pmatrix} \quad \mathbf{G} = \begin{pmatrix} Duv \\ Dvv + \frac{1}{2}gD^2 \\ Dvw \end{pmatrix} \quad \mathbf{H} = \begin{pmatrix} u\omega \\ v\omega \\ w\omega \end{pmatrix} \tag{13}$$

The source terms are given by

$$\mathbf{S}_h = \begin{pmatrix} gD\frac{\partial h}{\partial x} \\ gD\frac{\partial h}{\partial y} \\ 0 \end{pmatrix} \quad \mathbf{S}_p = \begin{pmatrix} -\frac{D}{\rho}(\frac{\partial p}{\partial x} + \frac{\partial p}{\partial \sigma}\frac{\partial \sigma}{\partial x^*}) \\ -\frac{D}{\rho}(\frac{\partial p}{\partial y} + \frac{\partial p}{\partial \sigma}\frac{\partial \sigma}{\partial y^*}) \\ -\frac{1}{\rho}\frac{\partial p}{\partial \sigma} \end{pmatrix} \quad \mathbf{S}_\tau = \begin{pmatrix} DS_{\tau_x} \\ DS_{\tau_y} \\ DS_{\tau_z} \end{pmatrix} \tag{14}$$

where the total pressure $\tilde{p} = p + \rho g(\eta - z^*)$ has been divided into it's dynamic (p) and hydrostatic ($\rho g(\eta - z^*)$) parts. It has been noted in a number of previous studies that the application of standard finite volume Godunov-type scheme directly to equations of this form does not lead to an automatic preservation of steady state (Zhou et al., 2001; Kim et al, 2008; Liang and Marche, 2009). Therefore, It is desirable to reformulate the equations so that the flux and source terms can be automatically balanced at the discrete level in the steady state. Following Shi et al. (2012), the source term is rewritten as

$$g(h+\eta)\frac{\partial h}{\partial x} = \frac{\partial}{\partial x}\left(\frac{1}{2}gh^2\right) + g\eta\frac{\partial h}{\partial x} \tag{15}$$

in which the first term in the right hand side can be combined together with the flux terms. Based on this, the flux terms $\mathbf{F}$ and $\mathbf{G}$ and source term $\mathbf{S_h}$ are rewritten as

$$\mathbf{F} = \begin{pmatrix} Duu + \frac{1}{2}g\eta^2 + gh\eta \\ Duv \\ Duw \end{pmatrix} \quad \mathbf{G} = \begin{pmatrix} Duv \\ Dvv + \frac{1}{2}g\eta^2 + gh\eta \\ Dvw \end{pmatrix} \quad \mathbf{S}_h = \begin{pmatrix} g\eta\frac{\partial h}{\partial x} \\ g\eta\frac{\partial h}{\partial y} \\ 0 \end{pmatrix} \tag{16}$$

The main advantage of the above formulation is that the flux and source terms are well-balanced so that no artificial flow due to bottom slope will be generated.

For the present landslide tsunami application, turbulent diffusion terms $S_{\tau_x}, S_{\tau_y}, S_{\tau_z}$ are neglected.

2 Numerical method

2.1 Grid configuration

A combined finite-volume and finite-difference scheme with a Godunov-type method was applied to discretize equations (9) and (12). It is straightforward to define all dependent variables at cell

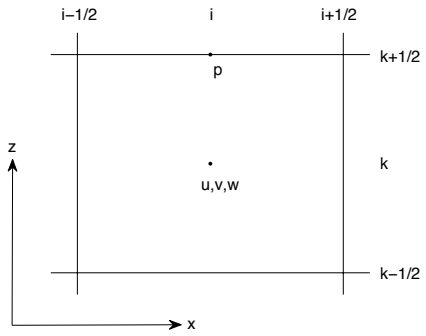

Figure 1: Layout of computational variables. Velocities (u, v, w) are placed at cell center and dynamic pressure p is defined at vertical cell face.

centers to solve the Riemann problem. However, this treatment results in checkerboard solutions in which the pressure and velocity become decoupled when they are defined at the same location (Patankar, 1980). Therefore, most existing models use a staggered grid in which the pressure is defined at the centers of computational cells and the velocities are defined at cell faces (Bradford, 2005). However, staggered grids do not lend themselves as easily as co-located grids to the use of Godunov-type schemes. Meanwhile, difficulty in treating the cell-centered pressure at the top layer may arise when applying the pressure boundary condition at the free surface (Yuan and Wu, 2004).

With these considerations, a different kind of staggered grid framework is introduced, in which the velocities are placed at the cell centers and the pressure is defined at the vertically-facing cell faces as shown in figure 1. The momentum equations are solved by a second-order Godunov-type finite volume method. The HLL approximate Riemann solver (Harten et al., 1983) is used to estimate fluxes at the cell faces. As in Stelling and Zijlema (2003), the pressure boundary condition at the free surface can be precisely assigned to zero.

2.2 Time Stepping

To obtain second-order temporal accuracy, the two-stage second-order nonlinear Strong Stability-Preserving (SSP) Runge-Kutta scheme (Gottlieb et al., 2001) is adopted for time stepping. At the first stage, an intermediate quantity $\mathbf{U}^{(1)}$ is evaluated using a typical first-order, two-step projection

method given by

$$\frac{\mathbf{U}^* - \mathbf{U}^n}{\Delta t} = -\left(\frac{\partial \mathbf{F}}{\partial x} + \frac{\partial \mathbf{G}}{\partial y} + \frac{\partial \mathbf{H}}{\partial \sigma}\right)^n + \mathbf{S}_h^n + \mathbf{S}_\tau^n \tag{17}$$

$$\frac{\mathbf{U}^{(1)} - \mathbf{U}^*}{\Delta t} = \mathbf{S}_p^{(1)} \tag{18}$$

where $\mathbf{U}^n$ represents $\mathbf{U}$ value at time level n, $\mathbf{U}^*$ is the intermediate value in the two-step projection method, and $\mathbf{U}^{(1)}$ is the final first stage estimate. In the second stage, the velocity field is again updated to a second intermediate level using the same projection method, after which the Runge-Kutta algorithm is used to obtain a final value of the solution at the $n+1$ time level.

$$\frac{\mathbf{U}^* - \mathbf{U}^{(1)}}{\Delta t} = -\left(\frac{\partial \mathbf{F}}{\partial x} + \frac{\partial \mathbf{G}}{\partial y} + \frac{\partial \mathbf{H}}{\partial \sigma}\right)^{(1)} + \mathbf{S}_h^{(1)} + \mathbf{S}_\tau^{(1)} \tag{19}$$

$$\frac{\mathbf{U}^{(2)} - \mathbf{U}^*}{\Delta t} = \mathbf{S}_p^{(2)} \tag{20}$$

$$\mathbf{U}^{n+1} = \frac{1}{2}\mathbf{U}^n + \frac{1}{2}\mathbf{U}^{(2)} \tag{21}$$

Each stage of the calculation requires the specification of the nonhydrostatic component of the pressure force as expressed through the quantities $\mathbf{S}_p^{(1,2)}$. The pressure field needed to specify these is based on the solution of the Poisson equation described below. Also at each stage, the surface elevation is obtained by solving equation (11) explicitly. The time step Δt is adaptive during the simulation, following the Courant-Friedrichs-Lewy (CFL) criterion

$$\Delta t = C\min\left[\min\frac{\Delta x}{|u_{i,j,k}| + \sqrt{gD_{i,j}}}, \min\frac{\Delta y}{|v_{i,j,k}| + \sqrt{gD_{i,j}}}, \min\frac{\Delta\sigma D_{i,j}}{|w_{i,j,k}|}\right] \tag{22}$$

where C is the Courant number, which is taken to be 0.5 to ensure accuracy and stability in the current model.

2.3 Spatial finite volume scheme

Equation (9) and (12) are discretized using a second-order Godunov-type finite volume method. To solve equation (9) and (12), fluxes based on the conservative variables are required at the cell faces. In high-order Godunov-type methods, the values of the conservative variables within a cell are calculated using a reconstruction method based on the cell center data (Zhou et al., 2001). Usually a piecewise linear reconstruction is used, leading to a second order scheme. For $\mathbf{U}$ in the cell i, we have

$$\mathbf{U} = \mathbf{U}_i + (x - x_i)\Delta\mathbf{U}_i \tag{23}$$

where $\Delta\mathbf{U}_i$ is the gradient of $\mathbf{U}$, which is calculated by

$$\Delta\mathbf{U}_i = \text{avg}\left(\frac{\mathbf{U}_{i+1} - \mathbf{U}_i}{x_{i+1} - x_i}, \frac{\mathbf{U}_i - \mathbf{U}_{i-1}}{x_i - x_{i-1}}\right) \tag{24}$$

in which avg is a slope limiter which is used to avoid spurious oscillations in the reconstruction data at the cell faces. In NHWAVE, the van Leer limiter is adopted, which is given by

$$\text{avg}(a,b) = \frac{a|b| + |a|b}{|a| + |b|} \tag{25}$$

The left and right values of $\mathbf{U}$ at cell face $(i + \frac{1}{2})$ are given by

$$\mathbf{U}^L_{i+\frac{1}{2}} = \mathbf{U}_i + \frac{1}{2}\Delta x_i \Delta \mathbf{U}_i \quad \mathbf{U}^R_{i+\frac{1}{2}} = \mathbf{U}_{i+1} - \frac{1}{2}\Delta x_{i+1}\Delta \mathbf{U}_{i+1} \tag{26}$$

The flux $\mathbf{F}(\mathbf{U}^L, \mathbf{U}^R)$ is calculated by solving a local Riemann problem at each horizontally-facing cell face. In the present study, HLL Riemann solver is employed. The flux at the cell interface $(i + \frac{1}{2})$ is determined by

$$\mathbf{F}(\mathbf{U}^L, \mathbf{U}^R) = \begin{cases} \mathbf{F}(\mathbf{U}^L) & \text{if} \quad s_L \geq 0 \\ \mathbf{F}^*(\mathbf{U}^L, \mathbf{U}^R) & \text{if} \quad s_L < 0 < s_R \\ \mathbf{F}(\mathbf{U}^R) & \text{if} \quad s_R \leq 0 \end{cases} \tag{27}$$

where

$$\mathbf{F}^*(\mathbf{U}^L, \mathbf{U}^R) = \frac{s_R \mathbf{F}(\mathbf{U}^L) - s_L \mathbf{F}(\mathbf{U}^R) + s_L s_R (\mathbf{U}^R - \mathbf{U}^L)}{s_R - s_L} \tag{28}$$

with wave speed s_L and s_R defined by

$$s_L = \min(u^L - \sqrt{gD_L}, u_s - \sqrt{gD_s}) \tag{29}$$

$$s_R = \max(u^R + \sqrt{gD_R}, u_s + \sqrt{gD_s}) \tag{30}$$

where u_s and $\sqrt{gD_s}$ are estimated by

$$u_s = \frac{1}{2}(u^L + u^R) + \sqrt{gD_L} - \sqrt{gD_R} \tag{31}$$

$$\sqrt{gD_s} = \frac{\sqrt{gD_L} + \sqrt{gD_R}}{2} + \frac{u^L - u^R}{4} \tag{32}$$

To obtain the non-hydrostatic velocity field, the dynamic pressure p has to be calculated first. From equation (18) and (20), we get

$$u^{(k)} = u^* - \frac{\Delta t}{\rho}\left(\frac{\partial p}{\partial x} + \frac{\partial p}{\partial \sigma}\frac{\partial \sigma}{\partial x^*}\right)^{(k)} \tag{33}$$

$$v^{(k)} = v^* - \frac{\Delta t}{\rho}\left(\frac{\partial p}{\partial y} + \frac{\partial p}{\partial \sigma}\frac{\partial \sigma}{\partial y^*}\right)^{(k)} \tag{34}$$

$$w^{(k)} = w^* - \frac{\Delta t}{\rho}\frac{1}{D^{(k)}}\frac{\partial p^{(k)}}{\partial \sigma} \tag{35}$$

where $k = 1, 2$ represents the kth stage in the Runge-Kutta integration.

Substituting equation (33) - (35) into the continuity equation (7), we obtain the Poisson equation in (x, y, σ) coordinate system, given by

$$\begin{aligned}
&\frac{\partial}{\partial x}\left[\frac{\partial p}{\partial x}+\frac{\partial p}{\partial \sigma}\frac{\partial \sigma}{\partial x^*}\right]+\frac{\partial}{\partial y}\left[\frac{\partial p}{\partial y}+\frac{\partial p}{\partial \sigma}\frac{\partial \sigma}{\partial y^*}\right]+\frac{\partial}{\partial \sigma}\left(\frac{\partial p}{\partial x}\right)\frac{\partial \sigma}{\partial x^*}+\\
&\frac{\partial}{\partial \sigma}\left(\frac{\partial p}{\partial y}\right)\frac{\partial \sigma}{\partial y^*}+\left[\left(\frac{\partial \sigma}{\partial x^*}\right)^2+\left(\frac{\partial \sigma}{\partial y^*}\right)^2+\frac{1}{D^2}\right]\frac{\partial}{\partial \sigma}\left(\frac{\partial p}{\partial \sigma}\right)=\\
&\frac{\rho}{\Delta t}\left(\frac{\partial u^*}{\partial x}+\frac{\partial u^*}{\partial \sigma}\frac{\partial \sigma}{\partial x^*}+\frac{\partial v^*}{\partial y}+\frac{\partial v^*}{\partial \sigma}\frac{\partial \sigma}{\partial y^*}+\frac{1}{D}\frac{\partial w^*}{\partial \sigma}\right)
\end{aligned} \tag{36}$$

The above equation is discretized using second-order space-centered finite differences. The velocities (u^*, v^*, w^*) at vertical cell faces are interpolated from adjacent cell-centered values. The resulting linear equation is given by

$$\begin{aligned}
&a_1 p_{i,j-1,k-1}+a_2 p_{i-1,j,k-1}+a_3 p_{i,j,k-1}+a_4 p_{i+1,j,k-1}+a_5 p_{i,j+1,k-1}+\\
&a_6 p_{i,j-1,k}+a_7 p_{i-1,j,k}+a_8 p_{i,j,k}+a_9 p_{i+1,j,k}+a_{10} p_{i,j+1,k}+a_{11} p_{i,j-1,k+1}+\\
&a_{12} p_{i-1,j,k+1}+a_{13} p_{i,j,k+1}+a_{14} p_{i+1,j,k+1}+a_{15} p_{i,j+1,k+1}=R_p
\end{aligned} \tag{37}$$

where

$$a_1 = -\left(\frac{(\sigma_y)_{i,j-1,k}}{2\Delta y(\Delta\sigma_k+\Delta\sigma_{k-1})}+\frac{(\sigma_y)_{i,j,k}}{2\Delta y(\Delta\sigma_k+\Delta\sigma_{k-1})}\right)$$

$$a_2 = -\left(\frac{(\sigma_x)_{i-1,j,k}}{2\Delta x(\Delta\sigma_k+\Delta\sigma_{k-1})}+\frac{(\sigma_x)_{i,j,k}}{2\Delta x(\Delta\sigma_k+\Delta\sigma_{k-1})}\right)$$

$$a_3 = -\frac{(\sigma_x^2+\sigma_y^2+\frac{1}{D^2})_{i,j,k}}{0.5(\Delta\sigma_k+\Delta\sigma_{k-1})\Delta\sigma_{k-1}}$$

$$a_4 = \frac{(\sigma_x)_{i+1,j,k}}{2\Delta x(\Delta\sigma_k+\Delta\sigma_{k-1})}+\frac{(\sigma_x)_{i,j,k}}{2\Delta x(\Delta\sigma_k+\Delta\sigma_{k-1})}$$

$$a_5 = \frac{(\sigma_y)_{i,j+1,k}}{2\Delta y(\Delta\sigma_k+\Delta\sigma_{k-1})}+\frac{(\sigma_y)_{i,j,k}}{2\Delta y(\Delta\sigma_k+\Delta\sigma_{k-1})}$$

$$a_6 = a_{10} = -\frac{1}{\Delta y^2} \quad a_7 = a_9 = -\frac{1}{\Delta x^2}$$

$$a_8 = \frac{2}{\Delta x^2}+\frac{2}{\Delta y^2}+\frac{(\sigma_x^2+\sigma_y^2+\frac{1}{D^2})_{i,j,k}}{0.5(\Delta\sigma_k+\Delta\sigma_{k-1})\Delta\sigma_k}+\frac{(\sigma_x^2+\sigma_y^2+\frac{1}{D^2})_{i,j,k}}{0.5(\Delta\sigma_k+\Delta\sigma_{k-1})\Delta\sigma_{k-1}}$$

$$a_{11} = \frac{(\sigma_y)_{i,j-1,k}}{2\Delta y(\Delta\sigma_k+\Delta\sigma_{k-1})}+\frac{(\sigma_y)_{i,j,k}}{2\Delta y(\Delta\sigma_k+\Delta\sigma_{k-1})}$$

$$a_{12} = \frac{(\sigma_x)_{i-1,j,k}}{2\Delta x(\Delta\sigma_k+\Delta\sigma_{k-1})}+\frac{(\sigma_x)_{i,j,k}}{2\Delta x(\Delta\sigma_k+\Delta\sigma_{k-1})}$$

$$a_{13} = -\frac{(\sigma_x^2 + \sigma_y^2 + \frac{1}{D^2})_{i,j,k}}{0.5(\Delta\sigma_k + \Delta\sigma_{k-1})\Delta\sigma_k}$$

$$a_{14} = -\left(\frac{(\sigma_x)_{i+1,j,k}}{2\Delta x(\Delta\sigma_k + \Delta\sigma_{k-1})} + \frac{(\sigma_x)_{i,j,k}}{2\Delta x(\Delta\sigma_k + \Delta\sigma_{k-1})}\right)$$

$$a_{15} = -\left(\frac{(\sigma_y)_{i,j+1,k}}{2\Delta y(\Delta\sigma_k + \Delta\sigma_{k-1})} + \frac{(\sigma_y)_{i,j,k}}{2\Delta y(\Delta\sigma_k + \Delta\sigma_{k-1})}\right)$$

$$R_p = -\frac{\rho}{\Delta t}\left(\frac{\partial u^*}{\partial x} + \frac{\partial u^*}{\partial \sigma}\frac{\partial \sigma}{\partial x^*} + \frac{\partial v^*}{\partial y} + \frac{\partial v^*}{\partial \sigma}\frac{\partial \sigma}{\partial y^*} + \frac{1}{D}\frac{\partial w^*}{\partial \sigma}\right)$$

where $\sigma_x = \frac{\partial \sigma}{\partial x^*}$ and $\sigma_y = \frac{\partial \sigma}{\partial y^*}$.

Uniform gridding is used in the horizontal direction while gridding in the vertical direction is generalized to be non-uniform in order to capture the bottom and surface boundary layers when desired. The coefficient matrix is asymmetric and has a total of 15 diagonal lines. The linear system is solved using the high performance preconditioner HYPRE software library. With p solved, the non-hydrostatic velocities at each stage can be updated from equation (33) to (35).

2.4 Boundary conditions

Boundary conditions are required for all the physical boundaries in order to solve the governing equations. Kinematic constraints on the surface and bottom boundaries have been discussed previously and are given by equations (3) and (4).

At the free surface, the continuity of normal and tangential stresses is enforced. With wind effects absent, the tangential stress equals zero, resulting in

$$\frac{\partial u}{\partial \sigma}|_{z=\eta} = \frac{\partial v}{\partial \sigma}|_{z=\eta} = 0 \tag{38}$$

The zero pressure condition on the free surface is applied when the Poisson equation is solved.

$$p|_{z=\eta} = 0 \tag{39}$$

At the bottom, the normal velocity and the tangential stress are prescribed. The normal velocity w is imposed through the kinematic boundary condition (4). For the inviscid case considered here, we use free-slip boundary conditions on the bottom and impose a zero-tangential-stress condition

$$\frac{\partial u}{\partial \sigma}|_{z=-h} = \frac{\partial v}{\partial \sigma}|_{z=-h} = 0 \tag{40}$$

Note that a form of bottom shear stresses is also implemented in the model and is not described here in the present application.

The Neumann boundary condition is used for dynamic pressure, which is directly obtained from the governing equation for w.

$$\frac{\partial p}{\partial \sigma}|_{z=-h} = -\rho D\frac{dw}{dt}|_{z=-h} \tag{41}$$

where w at $z = -h$ is given by (37). In the application to an underwater landslide, we linearize the resulting boundary condition which gives

$$\frac{\partial p}{\partial \sigma}|_{z=-h} = \rho D \frac{\partial^2 h}{\partial t^2} \tag{42}$$

At the closed boundaries or vertical walls, free-slip boundary conditions are imposed, so that the normal velocity and the tangential stress are set to zero. The normal pressure gradient is zero. At inflow, both free surface and velocities calculated from the analytical solutions are specified. In the lateral direction, periodic boundary conditions can be applied. To facilitate the parallel implementation, we used two ghost cells at each boundaries. The boundary conditions are specified at the ghost cells.

3 Basic hydrodynamic considerations

There are two basic states which are required in ensuring that any numerical model works for predicting evolution and inundations. The first step is to ensuring that the model conserves mass; the second basic step is checking convergence of this numerical code to a asymptotic limit.

3.1 Mass conservation

Conservation of mass can be checked by calculating water volume at the beginning and at the end of the computation. This should be dine by integrating disturbed water depth $\eta(x, y, t)$ over the entire flow domain, i.e., if the flow domain extends from the maximum penetration during inundation $x = X_{max}$ to the outer location of the source region X_S, and $y = Y_{max}$ to Y_s, then the total displaced volume $V(t)$ is,

$$V(t) = \int_{X_{max}}^{X_S} \int_{Y_{max}}^{Y_S} \eta(x, y, t) dx dy \tag{43}$$

The integral of $\eta(x, y, t)$ should be used instead of the integral of the entire flow depth $h(x, y, t) = \eta(x, y, t) + d(x, y, t)$ where $d(x, y, t)$ is the undisturbed water depth, because the latter is likely to conceal errors in the calculation. Typically,$\eta << d$ at offshore integrating h will simply produce the entire volume of the flow domain and will mask errors. Note that testing of the conservation of mass as above involves placing a closed domain within reflective boundaries (Synolakis et al., 2007).

Calculations of conservation of mass has been done for all of the benchmark problems reviewed in this report such that the total initial displaced volume $V(t = 0)$ was within less than 1% of the total displaced volume at the end of the computation $V(t = T)$ where T represents the computation end time. It is assumed that the end of the computation is when the initial wave is entirely reflected and reached offshore. However, with few changes in Δx and Δy the conservation of mass can be improved.

	Maximum Runup		
Grid Size	$H/d = 0.045$	$H/d = 0.091$	$H/d = 0.181$
0.1	0.02305	0.04058	0.06314
0.05	0.02305	0.04059	0.06316
0.01	0.02305	0.04059	0.06316
0.005	0.02305	0.04059	0.06316

Table 1: Maximum runup for gauge 9 for different grid size.

3.2 Convergence

Convergence is the another basic hydrodynamic consideration that is checked for all of the benchmarks in this research. Actually this process is made by checking convergence of the numerical code to a certain asymptotic limit, presumably the actual solution of the equations solved. The grid steps Δx and Δy has been halved, and the time step Δt automatically reduced appropriately to conform to the Courant-Friedrics-Levy (CFL) criterion. As recommended in literature, convergence of the code has been checked through the extreme runup and rundown. Table 1 displays convergence of the code tested during the conical island test problem which is discussed in Section 5.3 below.

4 Analytical benchmark

In this section, we compare numerical results for solitary wave shoaling on a plane beach to an analytic solution based on the shallow water equations. The benchmark data for comparison are obtained from Synolakis et al (2007).

4.1 Solitary wave on a simple beach

The canonical problem of the shallow water-wave equations is covered here which contains the calculation of a long wave climbing up a sloping beach of angle β attached to a constant-depth region (Figure 2). The origin of the coordinate system is at the initial position of the shoreline and x increases seaward.

It is possible to derive exact results for the evolution and runup of solitary waves based on linear theory (Synolakis, 1986, 1987). Solitary waves have long been used as a model for the leading wave of tsunamis. Russell (1845) defined solitary waves as the great waves of translation, and consists of a single elevation wave. While capturing some of the basic physics of tsunamis, solitary waves do not model the physical manifestation of tsunamis in nature, which are invariably N-wave like with a leading-depression wave followed by an elevation wave (Synolakis et al., 2007). The following runup law for the maximum runup R is provided based on slope of the beach and wave height of

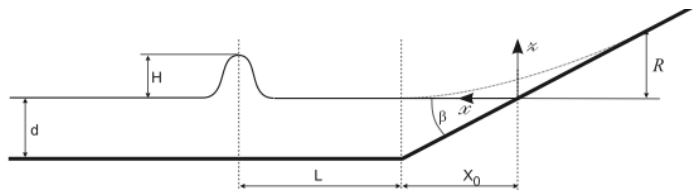

Figure 2: Definition sketch for simple beach bathymetry(from Synolakis et al (2007, Figure A1)).

				R/d		
d(m)	$\Delta x(m)$	H/d	$Cot(\beta)$	Runup Law	Numerical Calculations	Error(%)
0.5	0.1	0.03	10.0	0.112	0.113	0.9
0.5	0.1	0.05	10.0	0.212	0.207	2.4
0.5	0.1	0.1	3.333	0.291	0.281	3.2
5.0	1.0	0.03	10.0	0.112	0.111	0.9
5.0	1.0	0.05	10.0	0.212	0.209	1.2
5.0	1.0	0.10	3.372	0.308	0.302	2.1
5.0	1.0	0.10	3.372	0.731	0.723	1.1
100	5.0	0.03	2.747	0.600	0.596	0.7
100	5.0	0.03	20.0	0.040	0.040	1.0

Table 2: Runup data from numerical calculations compared with runup law values.

the solitary wave

$$R = 2.831\sqrt{\cot\beta}H^{\frac{5}{4}} \tag{44}$$

Benchmark problems that are studied here have different depths from 50cm to 1000m. Also, for each depth, different slopes and wave heights has been studied. Table 2 provides a list of selected examples that has been modeled including their maximum runup and the grid size for each case. Figure 3 defines a comparison between numerical simulation and runup law.

In addition, the analytical solution for different times is available for a specific case in which $H/d = 0.0019$ and $\beta = \text{arccot}(19.85)$. In order to have the same time with the data it was recommended that $L = \text{arccosh}(\sqrt{20})/\gamma$ in which $\gamma = \sqrt{3H/4d}$; therefore, the distance of the wave from initial shoreline(X_1) can be written as $X_1 = X_0 + L$ (with respect to Figure 2). Figure 4 demonstrates profiles and time series of the water in eight different times. Extreme positions of the shoreline are shown in figure 4 (the maximum runup and rundown occur $t \simeq 55(d/g)^{1/2}$ and $t \simeq 70(d/g)^{1/2}$). Figure 5 shows water level fluctuations at two gauge locations $X/d = 0.25$, $X/d = 9.95$. As it is clear in the figure the point $X/d = 0.25$ which is closer to initial shoreline, becomes temporarily dry during the process but the point $X/d = 9.95$ remains wet throughout the entire length of the numerical simulation.

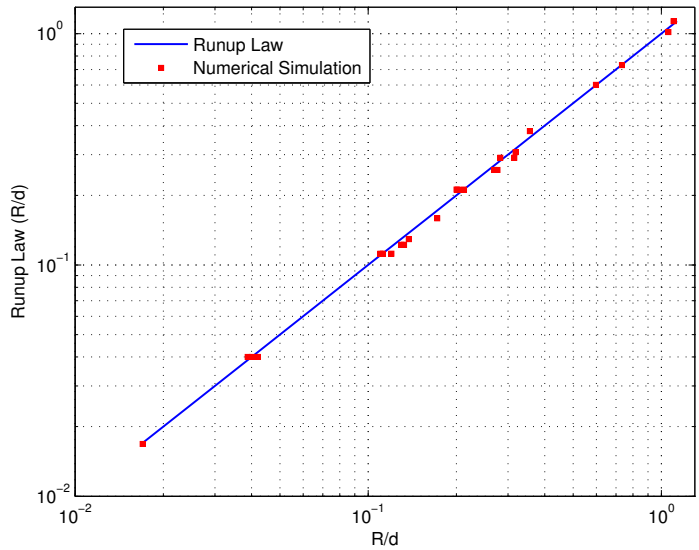

Figure 3: Numerical simulation data for maximum runup of nonbreaking waves climbing up different beach slopes. Solid line represents the runup law (25).

5 Laboratory benchmarks

In this section, four different laboratory benchmarks are studied, and results of numerical calculations are compared to laboratory data. The following benchmark problems are studied in this section: ,

1. Solitary wave on a simple beach
2. Solitary wave on a composite beach
3. Solitary wave on a conical island
4. Submarine landslide generation of tsunami

5.1 Solitary wave on a simple beach

In this laboratory test, the 31.73 m-long, 60.96 cm-deep and 39.97 cm wide California Institute of Technology, Pasadena, California wave tank was used with water at varying depths. The tank is described by Synolakis (1986, 1987). The bottom of the tank consisted of painted stainless steel

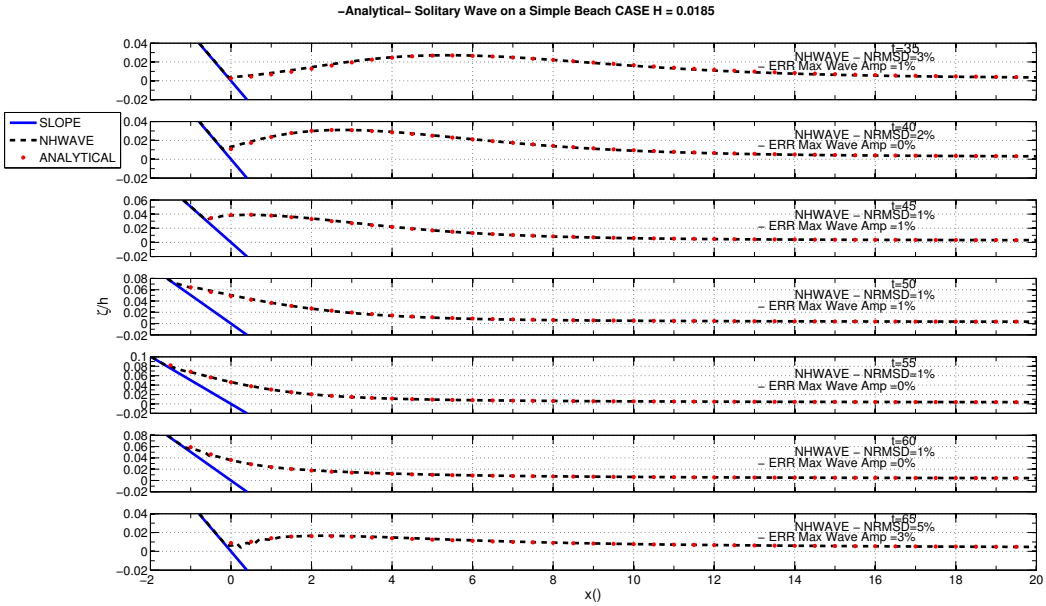

Figure 4: The water level profiles during runup of the non-breaking wave in the case of $H/d = 0.019$ on a 1:19.85 beach. Solid blue line represents the analytical solution in according to Synolakis(1986), and dashed red lines represents the numerical simulation.

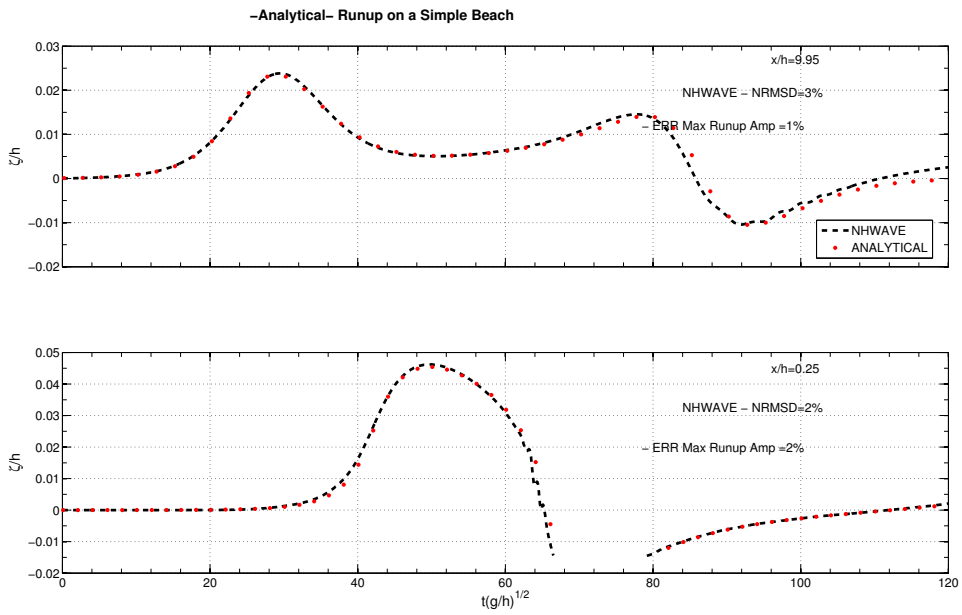

Figure 5: The water level dynamics at two locations $X/d = 0.25$ and $X/d = 9.95$. Solid blue line represents the analytical solution in according to Synolakis(1986), and dashed red line represents the numerical simulation.

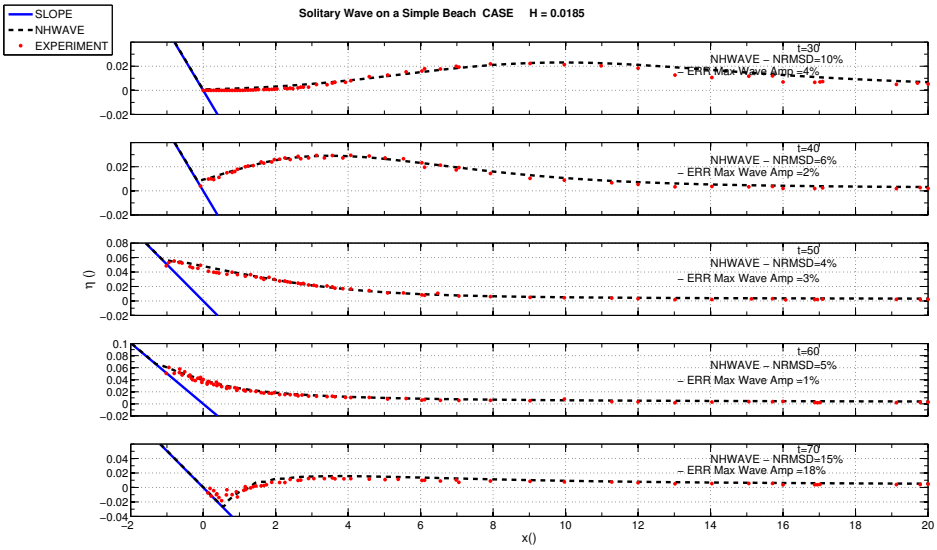

Figure 6: Time evolution of nonbreaking $H/d = 0.0185$ initial wave.

plates. A ramp was installed at one end of the tank to model the bathymetry of the canonical problem of a constant-depth region adjoining a sloping beach. The ramp had a slope of 1:19.85. The ramp was sealed to the tank side walls. The toe of the ramp was distant 14.95 m from the rest position of the piston generator used to generate waves.

This set of laboratory data has been vastly used for many code validations. In this modeling test, the data sets for the $\tilde{H}/\tilde{d} = 0.0185$ nonbreaking and $\tilde{H}/\tilde{d} = 0.30$ breaking solitary waves which are the most frequently used and most appropriate for code validation.

For these cases a grid size of $\Delta x = 0.05$ m and three layaer girds has been used. Figure 6 and Figure 7 displays the accuracy of the model for both nonbreaking and breaking waves.

5.2 Solitary wave on a composite beach

Revere Beach is located approximately 6 miles northeast of Boston in the City of Revere, Massachusetts. To address beach erosion and severe flooding problems, a physical model of the beach was constructed at the Coastal Engineering Laboratory of the U.S. Army Corps of Engineers, Vicksburg, Mississippi facility, earlier known as Coastal Engineering Research Center. This benchmark is described in Section 3.2 of Appendix A of Synolakis et al (2007).

In this benchmark problem a complex topography consisting of three segments and a vertical wall is considered (Figure 8). The benchmark test is described in Appendix A, Section 2.2 of

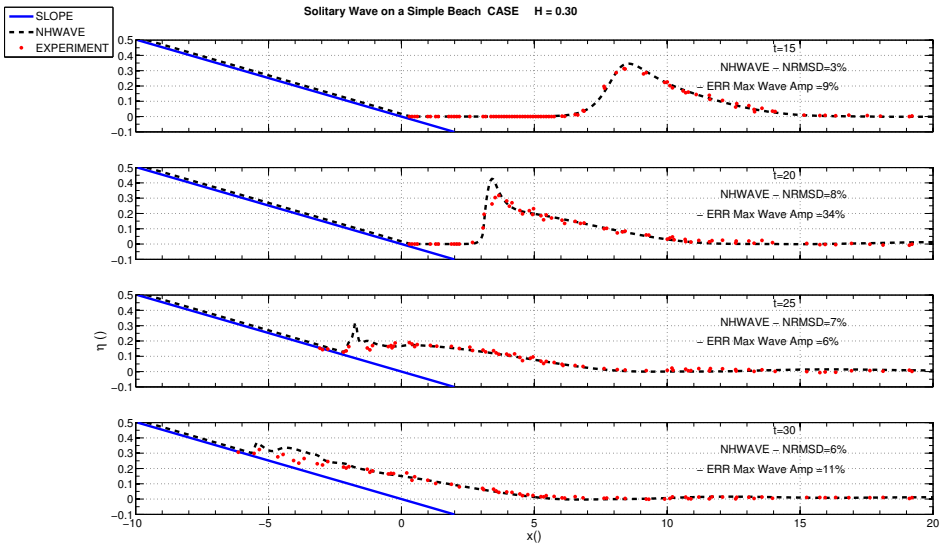

Figure 7: Time evolution of breaking $H/d = 0.3$ initial wave.

Synolakis et al (2007). Runup of non-breaking solitary waves on the vertical wall is simulated in this case. Results have been compared with the analytical solution. Laboratory data exist for this topography from a U.S. Army Corps of Engineers, Coastal Engineering Research Center, Vicksburg, Mississippi experiment of wave runup on a model of Revere Beach, Massachusetts. In this benchmark problem three different waves are modeled ($H/d = 0.0378, 0.2578, 0.6404$ for cases A, B and C) and the numerical data is compared with the laboratory data for gauges 4 to 10 in Figures 9 - 11). Grid size for this case is $\Delta x = 0.010$ m.

5.3 Solitary wave on a conical island

Laboratory experiments on the interaction between solitary waves and a conical island were conducted by Briggs et al (1995). The three cases from this test illustrate the important fact that runup and inundation heights on the sheltered back sides of an island can exceed the incident wave height on the exposed front side, due to trapping of wave fronts propagating around the island circumference. These tests have been used in a number of validation studies for a variety of models, including nonlinear shallow water equations (Liu et al 1995) and Boussinesq equations (Chen et al, 2000). The benchmark test is specified in Section 3.3 of Appendix A of Synolakis et al (2007).

Large-scale laboratory experiments were performed at Coastal Engineering Research Center, Vicksburg, Mississippi, in a 30m-wide, 25m-long, and 60cm-deep wave basin (Figure 12). In the

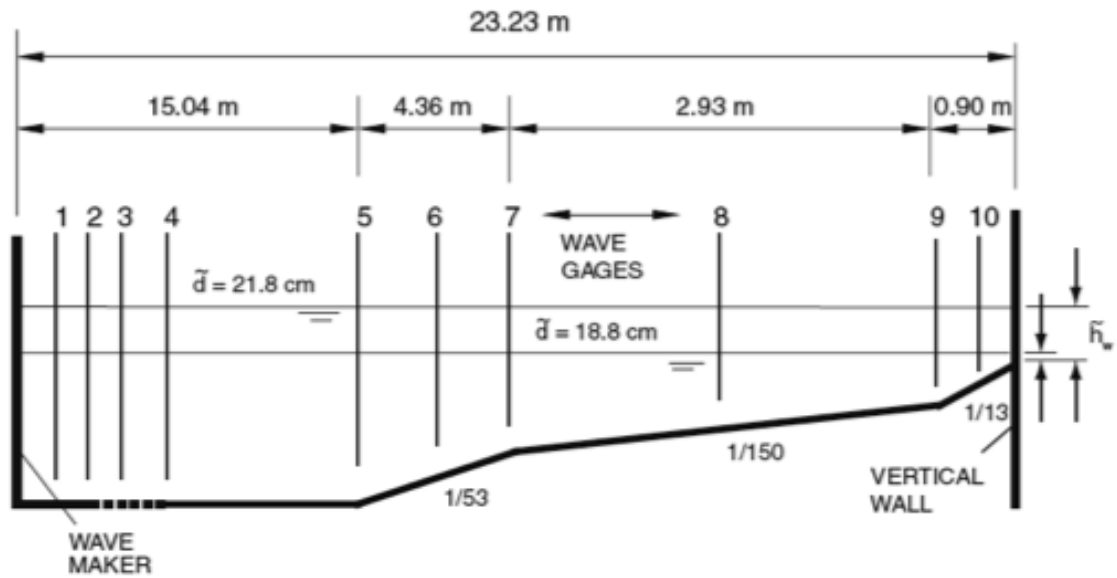

Figure 8: Definition sketch for Revere Beach (from Synolakis et al (2007, Figure A7)).

physical model, a 62.5cm-high, 7.2m toe-diameter, and 2.2m crest-diameter circular island with a 1:4 slope was located in the basin (Figure 13). Experiments were conducted at depth of 32cm, with three different solitary waves (H/d=0.045, 0.091, 0.181). Water-surface time histories were measured with 27 wave gages located around the perimeter of the island (Figure 14).

For this benchmark test, time histories of the surface elevation around the circular island are given at four locations, i.e., in the front of the island at the toe (Gauge 6) and gauges closest to the shoreline with the numbers 9, 16, and 22 located at the $0°$, $90°$, and $180°$ radial lines (Figure 14). A grid size of $\Delta x = 0.10m$ is considered for proper numerical simulation of this benchmark. Figures 15-17 shows the comparison between the laboratory data with numerical calculations.

5.4 3D underwater landslide

In this benchmark test we utilize the provided background information and details of available data, for a three dimensional (3D) underwater landslide tsunami laboratory benchmark that can be used for validating landslide tsunami models, based on Enet and Grilli's (2007) experiment (Figure 18). These experiments are performed on a plane incline with angle $\theta = 15^o$, using a smooth streamlined Gaussian-Shaped body, released at time $t = 0$ from different initial submergence depths (d) (Figure 19). Available measured includes slide kinematics, obtained from slide acceleration utiliz-

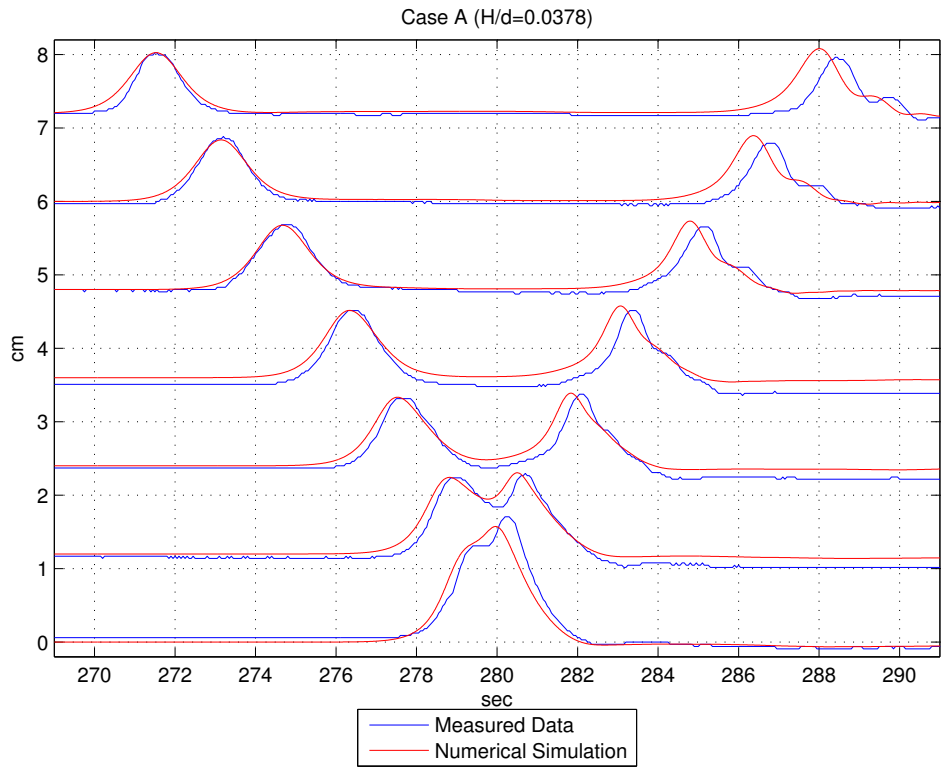

Figure 9: Time evolution of nonbreaking $H/d = 0.0378$ initial wave on composite beach. The red line shows the numerical solution and blue line represents the laboratory data.

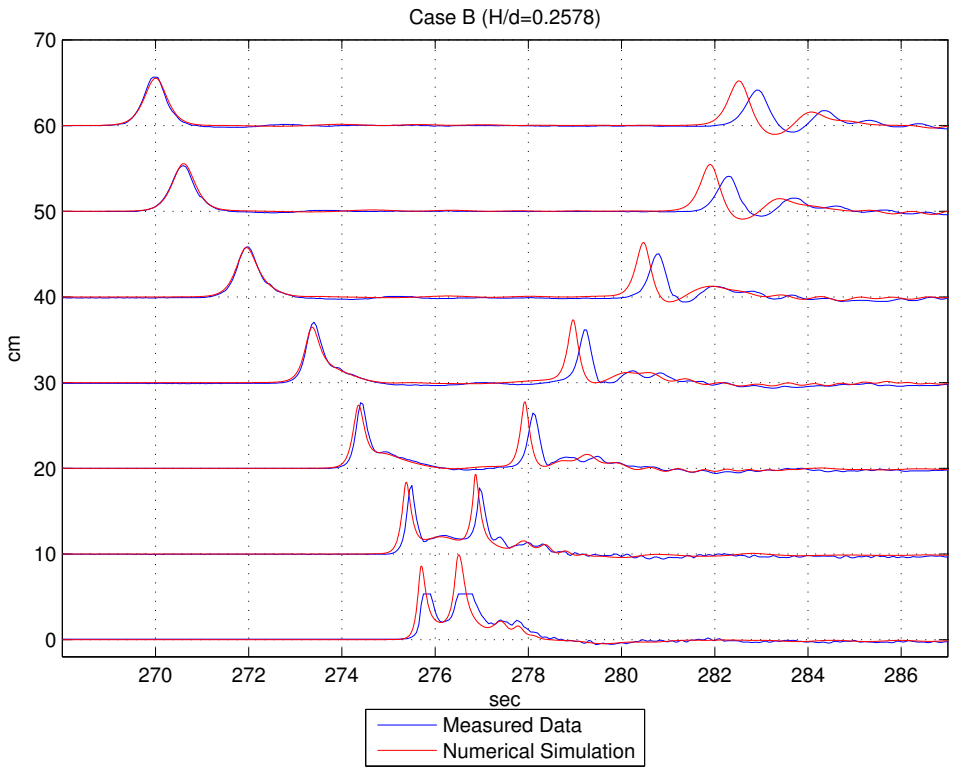

Figure 10: Time evolution of breaking $H/d = 0.2578$ initial wave on composite beach. The red line shows the numerical solution and blue line represents the laboratory data.

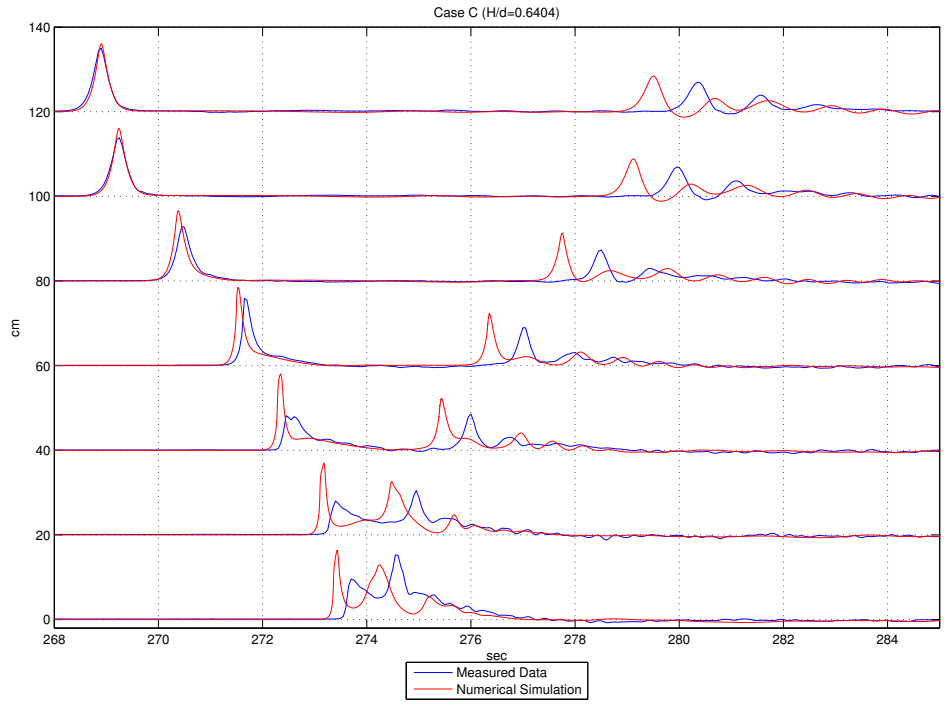

Figure 11: Time evolution of breaking $H/d = 0.6404$ initial wave on composite beach. The red line shows the numerical solution and blue line represents the laboratory data.

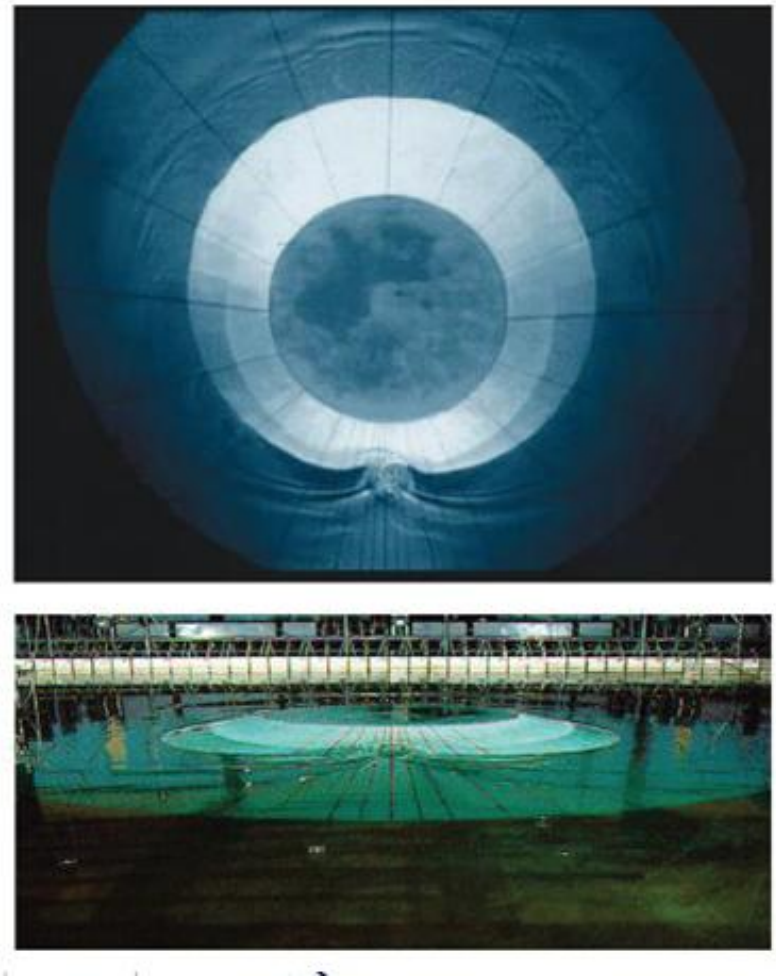

Figure 12: View of conical island(top) and basin(bottom)(from Synolakis et al (2007, Figure A16)).

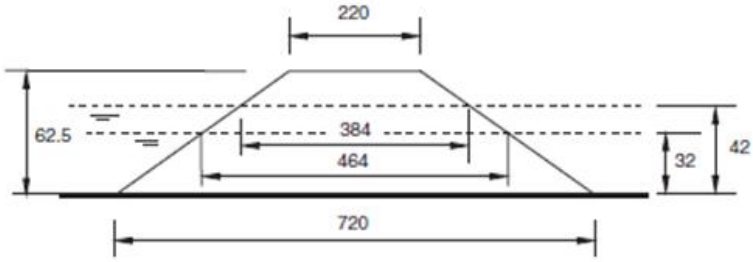

Figure 13: Definition sketch for conical island. All dimensions are in cm (from Synolakis et al (2007, Figure A17)).

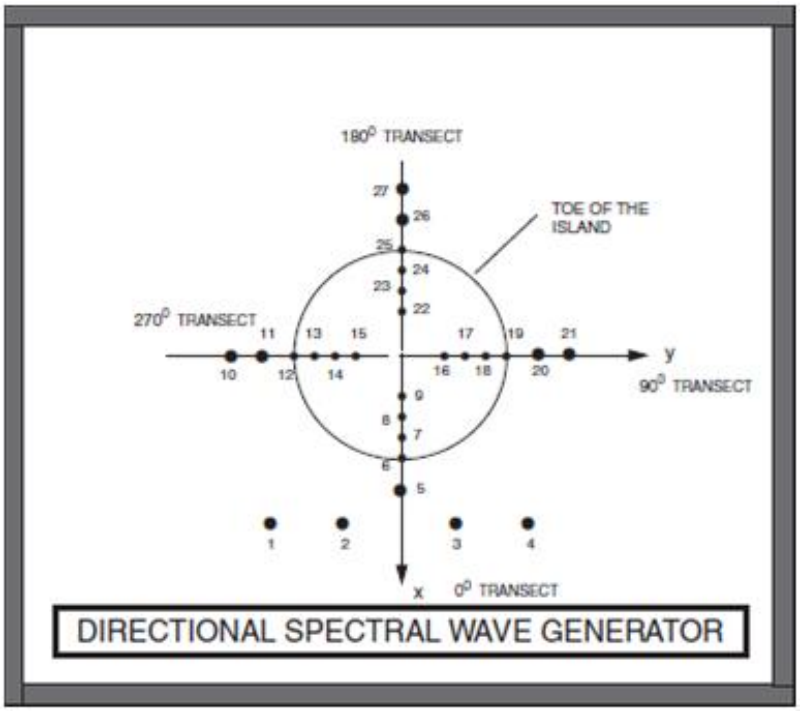

Figure 14: Schematic gauge locations around the conical island(from Synolakis et al (2007, Figure A18)).

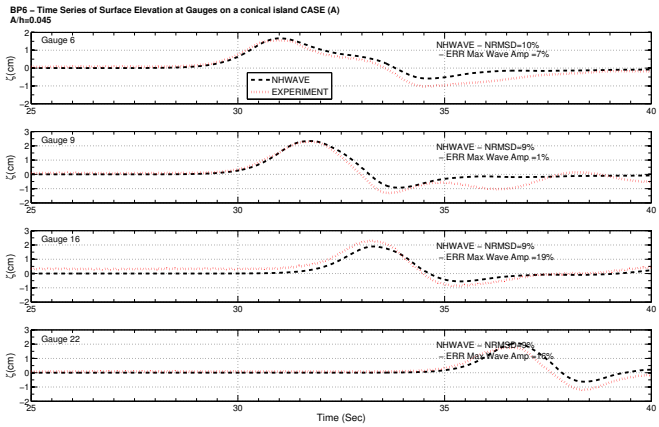

Figure 15: Comparison of computed and measured time series of free surface for $H/d = 0.045$.

Case	A	B	C	D	E	F	G
d (mm)	61	80	100	120	140	149	189
x_0(mm)(measured)	551	617	696	763	846	877	1017
x_0(mm)(theoretical)	560	630	705	780	854	888	1037
η_0(mm)	13.0	9.2	7.8	5.1	4.4	4.2	3.1
$a_0(m/s^2)$	1.20	1.21	1.19	1.17	1.14	1.20	1.21
$u_t(m/s)$	1.70	1.64	1.93	2.03	2.13	1.94	1.97

Table 3: Measure and curve-fitted slide and wave parameters for various initial submergence depths (Enet and Grilli, 2007)

ing a micro-accelerometer within the slide, time passage of the slide, and surface elevation for four gauges. Each experiments was repeated twice and both raw and averaged data was provided for each case.

Experimental Setup and slide geometry as well as slide kinematics are discussed in Enet and Grilli (2007). Table 3 demostrates the experimental parameters and measured data for seven different cases of the experiment. Figure 20 depicts guage locations for each experiment and Table 4 shows the coordinates of each gauge. Finally, Figures 21 - 27 show the comparison between measured data and simulated landslide for seven cases.

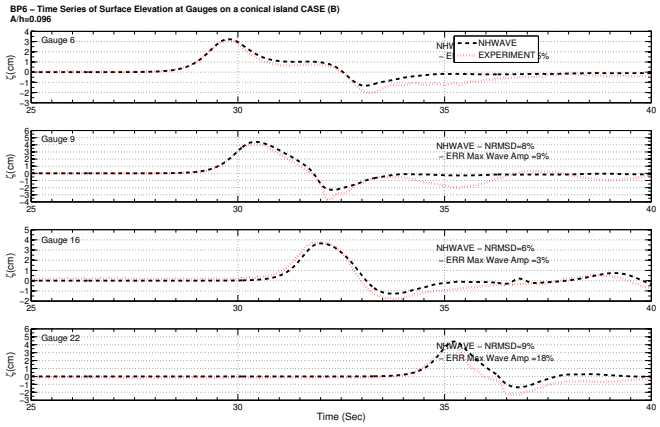

Figure 16: Comparison of computed and measured time series of free surface for $H/d = 0.091$.

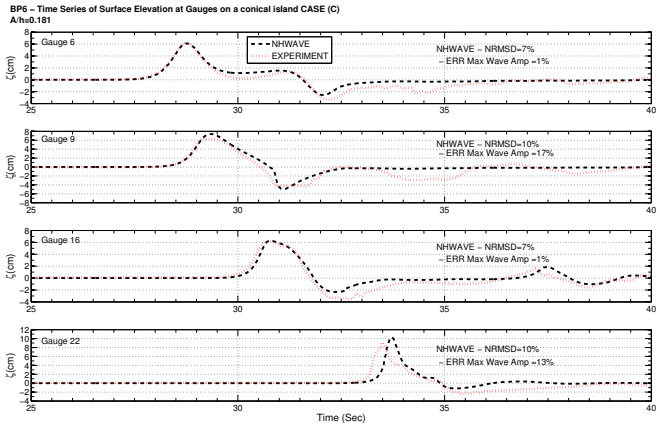

Figure 17: Comparison of computed and measured time series of free surface for $H/d = 0.181$.

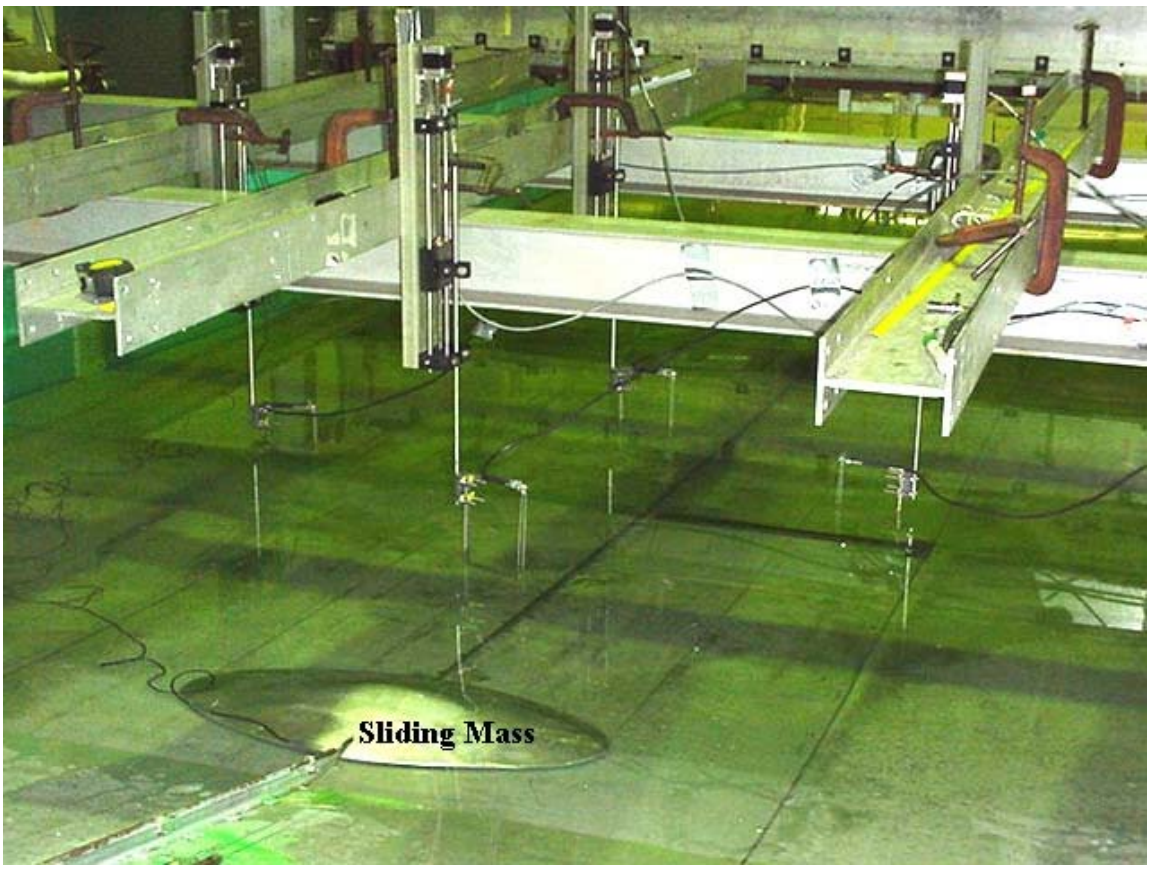

Figure 18: Experimental setup of under water landslide experiments (Enet and Grilli, 2007)

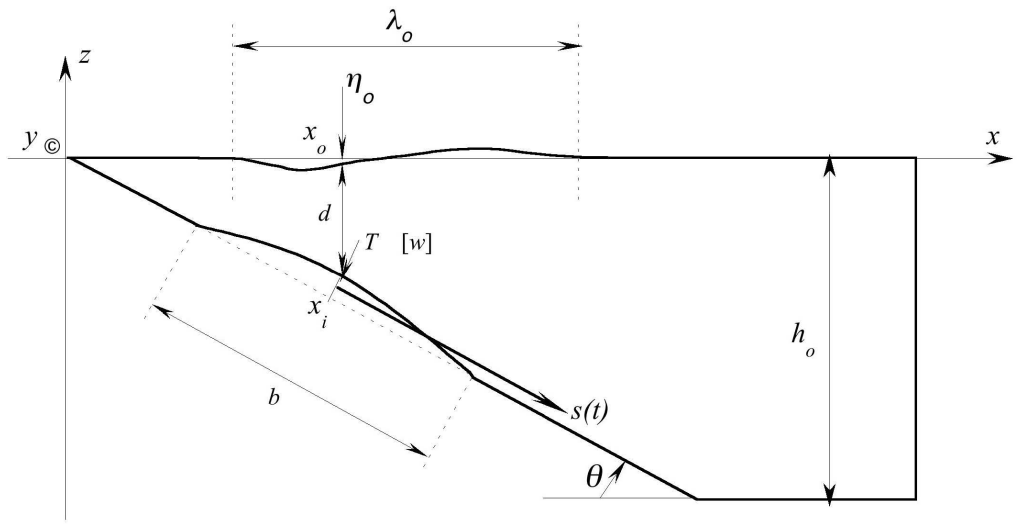

Figure 19: Vertical Cross section of underwater landslide (Enet and Grilli, 2007)

Gauge	1	2	3	4
(x, y) (mm)	$(x_0, 0)$	(1469,350)	(1929,0)	(1929,500)

Table 4: Wave Gauges Locations (Enet and Grilli, 2007)

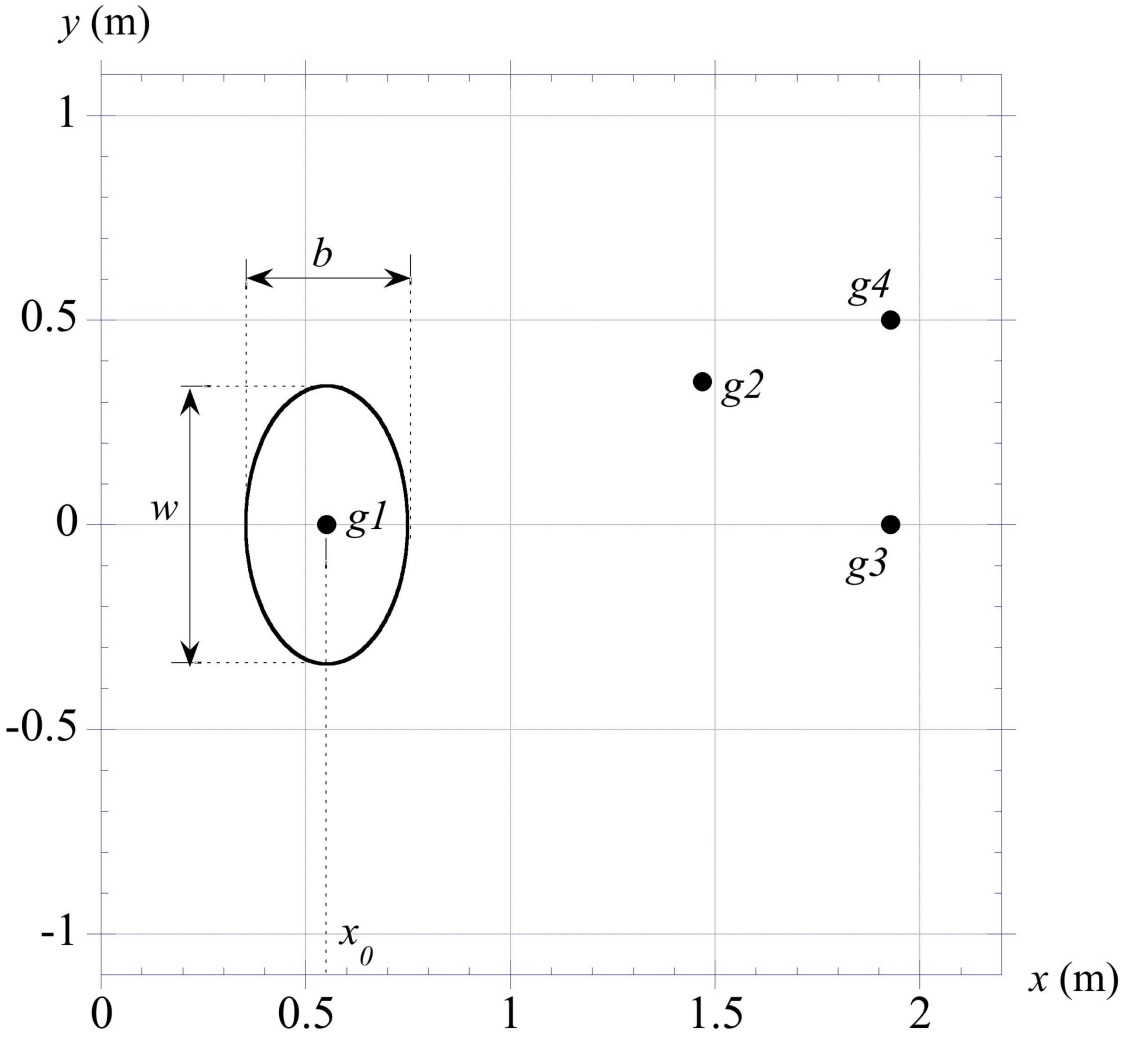

Figure 20: Landslide Gauge Locations (Table 4) (Enet and Grilli, 2007)

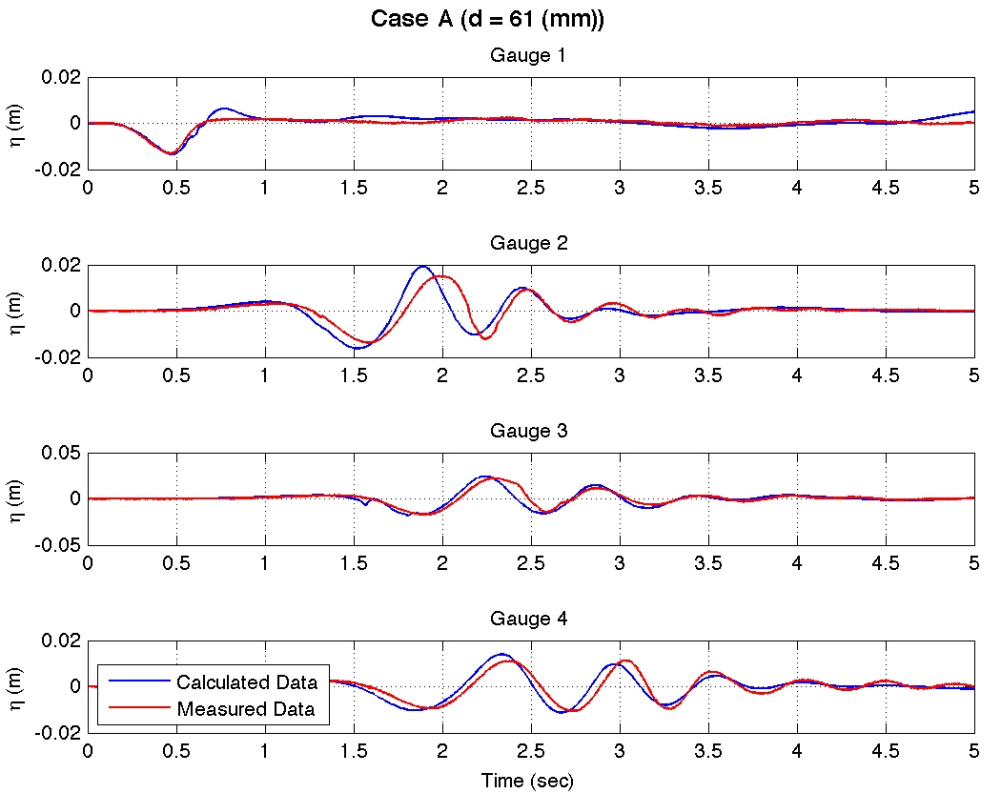

Figure 21: Surface elevation of measured and computed data (Case A)

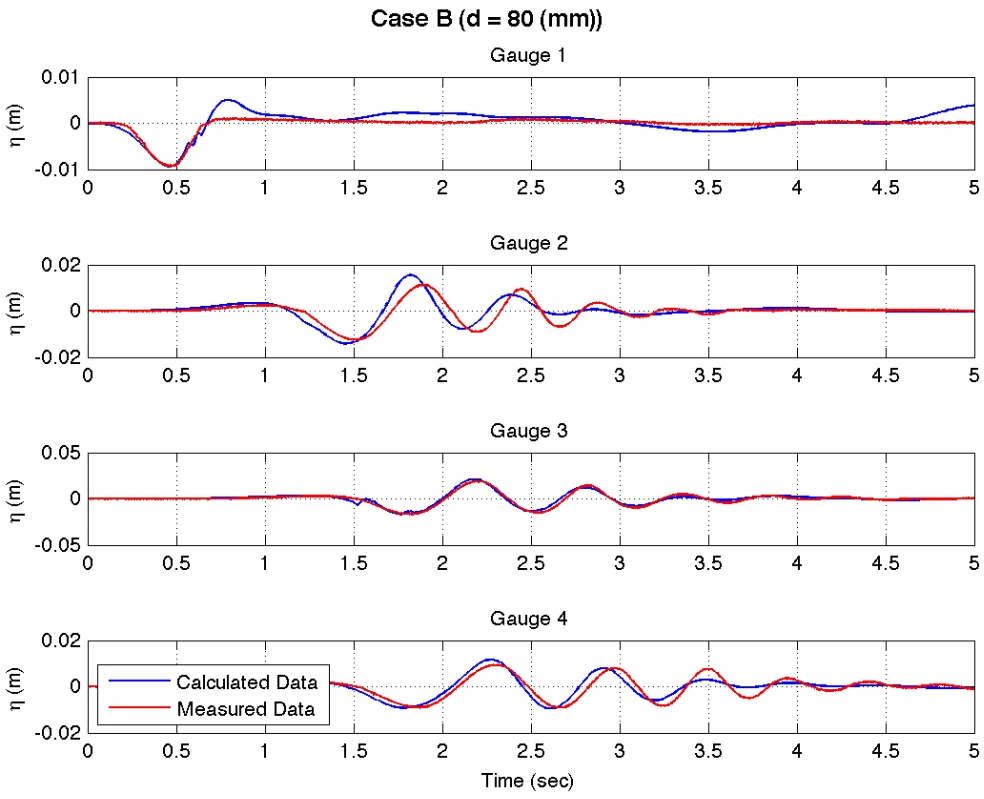

Figure 22: Surface elevation of measured and computed data (Case B)

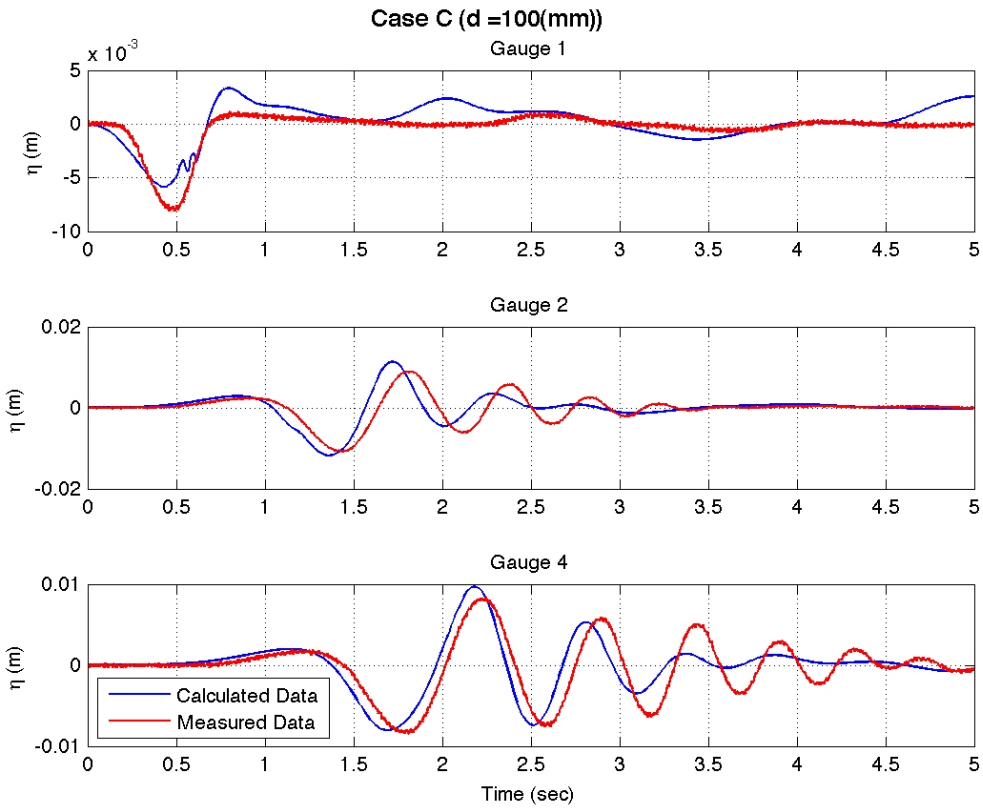

Figure 23: Surface elevation of measured and computed data (Case C)

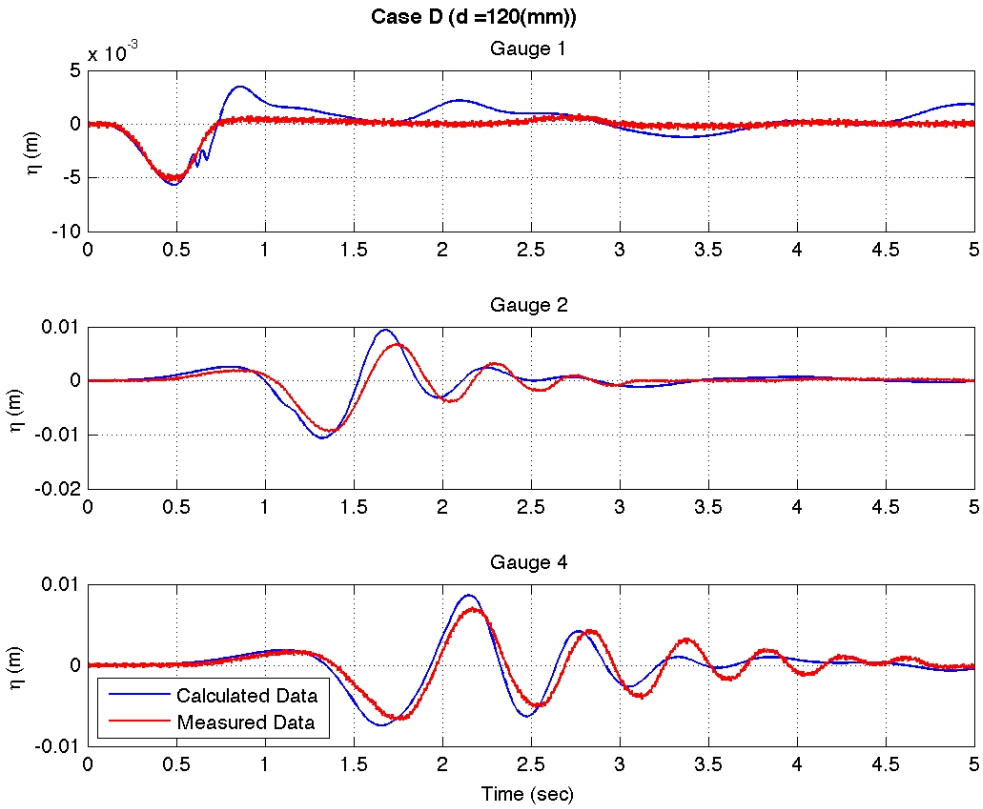

Figure 24: Surface elevation of measured and computed data (Case D)

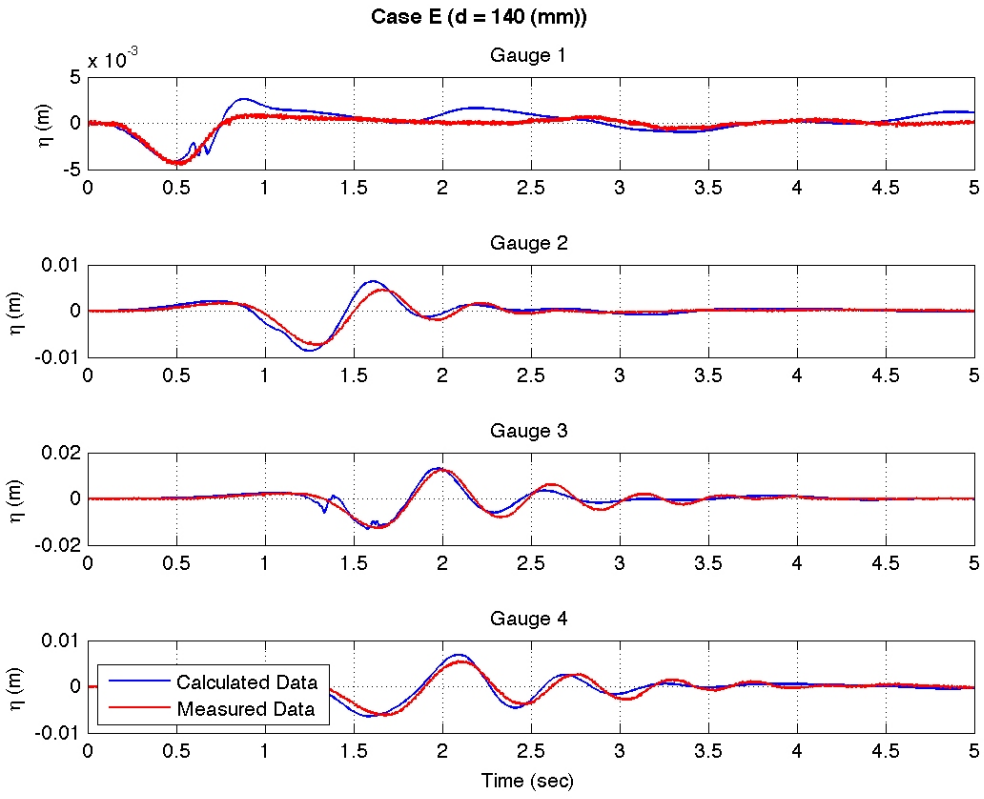

Figure 25: Surface elevation of measured and computed data (Case E)

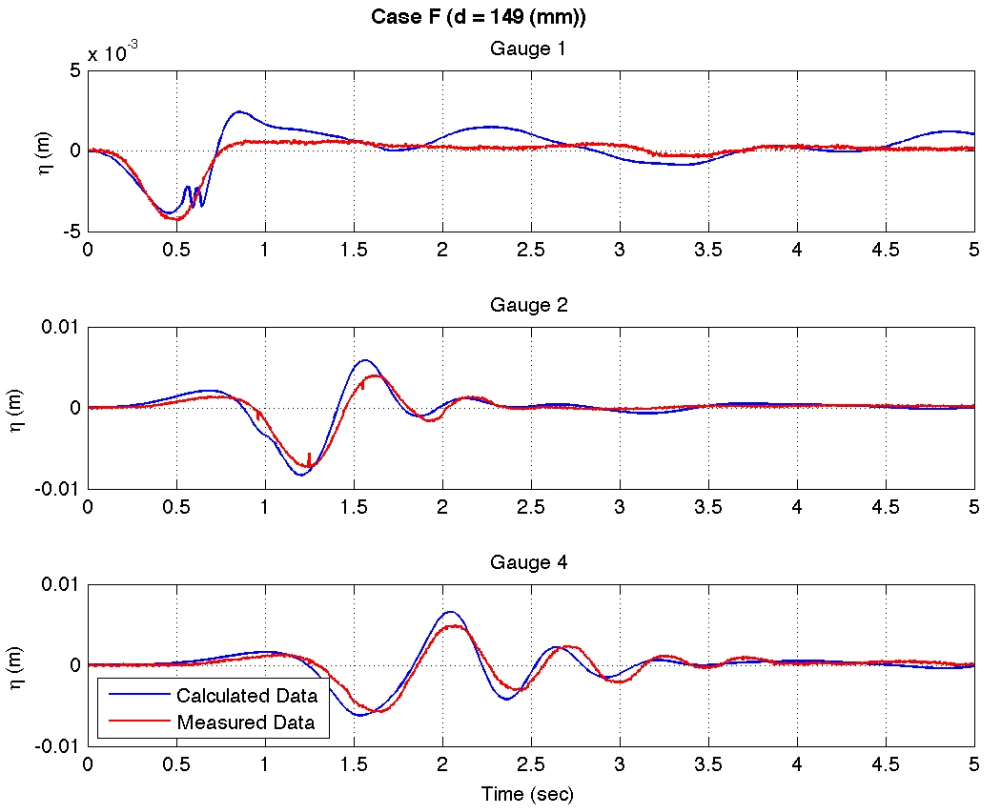

Figure 26: Surface elevation of measured and computed data (Case F)

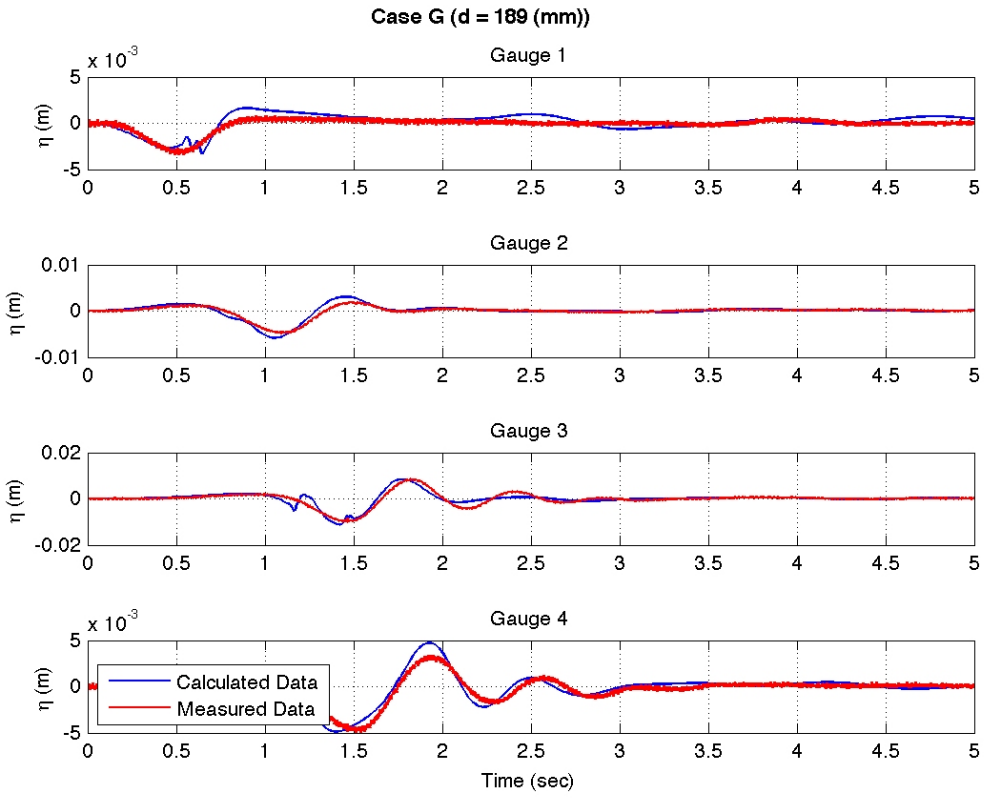

Figure 27: Surface elevation of measured and computed data (Case G)

References

Briggs, M. J., Synolakis, C. E., Harkins, G. S. and Green, D., 1995, "Laboratory experiments of tsunami runup on a circular island", *Pure Appl. Geophys.*, **144**, 569-593.

Chen, Q., Kirby, J. T., Dalrymple, R. A., Kennedy, A. B. and Chawla, A., 2000, "Boussinesq modelling of wave transformation, breaking and runup. II: Two horizontal dimensions", *J. Waterway, Port, Coast. Ocean Engnrng*, **126**, 48-56.

Chen, Q., Kirby, J. T., Dalrymple, R. A., Shi, F. and Thornton, E. B., 2003, "Boussinesq modelling of longshore currents", *J. Geophys. Res.*, **108**(C11), 3362, doi:10.1029/2002JC001308.

Chen, Q., 2006, "Fully nonlinear Boussinesq-type equations for waves and currents over porous beds", *J. Eng. Mech.*, **132**, 220-230.

Enet, F., Grilli, S.T., 2007, "Experimental Study of Tsunami Generation by Three-dimensional Rigid Underwater Landslides", *Journal of Waterway Port Coastal and Ocean Engineering*, **133**(6), 442-454.

Gottlieb, S., Shu C.-W., and Tadmore, E., 2001, "Strong stability-preserving high-order time discretization methods", *SIAM Review*, **43** (1), 89 - 112.

Kennedy, A. B., Kirby, J. T., Chen, Q. and Dalrymple, R. A., 2001, "Boussinesq-type equations with improved nonlinear performance", *Wave Motion*, **33**, 225-243.

Kim, D. H., Cho, Y. S. and Kim, H. J., 2008, "Well balanced scheme between flux and source terms for computation of shallow-water equations over irregular bathymetry", *J. Eng. Mech.*, **134**, 277-290.

Kirby, J. T., Wei, G., Chen, Q., Kennedy, A. B. and Dalrymple, R. A., 1998, " FUNWAVE 1.0, Fully nonlinear Boussinesq wave model. Documentation and user's manual", Research Report No. CACR-98-06, Center for Applied Coastal Research, University of Delaware.

Liang, Q. and Marche, F., 2009, "Numerical resolution of well-balanced shallow water equations with complex source terms", *Adv. Water Res.*, **32**, 873 - 884.

Liu, P. L.-F., Cho, Y. S., Briggs, M. S., Kânoğlu, U. and Synolakis, C. E., 1995, "Runup of solitary waves on a circular island", *J. Fluid Mech.*, **320**, 259-285.

Naik, N. H., Naik, V. K., and Nicoules, M., 1993, "Parallelization of a class of implicit finite difference schemes in computational fluid dynamics", *Int. J.High Speed Computing*, **5**, 1-50.

Nwogu, O., 1993, "An alternative form of the Boussinesq equations for nearshore wave propagation", *J. Waterway, Port, Coastal, and Ocean Engineering*, **119**, 618-638.

Roeber, V., Cheung, K. F., and Kobayashi, M. H., 2010, "Shock-capturing Boussinesq-type model for nearshore wave processes", *Coastal Engineering*, **57**, 407-423.

Rogers, B. D., Borthwick, A. G. L., and Taylor, P. H., 2003, "Mathematical balancing of flux gradient and source terms prior to using Roe's approximate Riemann solver", *J. Comp. Phys.*, **192**, 422-451.

Russel, J.S., 1845, "Report on waves", *Rp. Meet. Brit. Assoc. Adv. Sci. 14th*, 311? 390, John Murray, London.

Shi, F., Dalrymple, R. A., Kirby, J. T., Chen, Q. and Kennedy, A., 2001, "A fully nonlinear Boussinesq model in generalized curvilinear coordinates", *Coastal Engineering*, **42**, 337-358.

Shi, F., Kirby, J. T., Harris, J. C., Geiman, J. D. and Grilli, S. T., 2011a, "A high-order adaptive time-stepping TVD solver for Boussinesq modelling of breaking waves and coastal inundation", In Prepration for Ocean Modelling.

Shi, F., Kirby, J. T., Tehranirad, B., Harris, J. C. and Grilli, S. T., 2011b, "FUNWAVE-TVD Version 1.0. Fully nonlinear Boussinesq wave model with TVD solver. Documentation and user's manual", Research Report No. CACR-11-04, Center for Applied Coastal Research, University of Delaware.

Shiach, J. B. and Mingham, C. G., 2009, "A temporally second-order accurate Godunov-type scheme for solving the extended Boussinesq equations", *Coast. Eng.*, **56**, 32-45.

Synolakis, C.E., 1986, "The runup of long waves", Ph.D. Thesis, California Institute of Technology, Pasadena, California, 91125, 228 pp.

Synolakis, C.E., 1987, "The runup of solitary waves", *J. Fluid Mech.*, **185**, 523?545.

Synolakis, C. E., Bernard, E. N., Titov, V. V., Kânoğlu, U. and González, F. I., 2007, "Standards, criteria, and procedures for NOAA evaluation of tsunami numerical models", NOAA Tech. Memo. OAR PMEL-135, Pacific Marine Env. Lab., Seattle.

Tadepalli, S. and C.E. Synolakis, 1994, "The runup of N-waves on sloping beaches", *Proc. R. Soc. A*, **445**, 99-112.

Tonelli, M. and Petti, M., 2009, "Hybrid finite volume - finite difference scheme for 2DH improved Boussinesq equations", *Coast. Engrng.*, **56**, 609-620.

Wei, G., Kirby, J.T., Grilli, S.T., Subramanya, R., 1995, "A fully nonlinear Boussinesq model for surface waves: Part I. Highly nonlinear unsteady waves", *J. Fluid Mech.*, **294**, 71-92.

Yamamoto, S. and Daiguji, H., 1993, "Higher-order-accurate upwind schemes for solving the compressible Euler and Navier-Stokes equations", *Computers and Fluids*, **22**, 259-270.

Yamamoto, S., Kano, S. and Daiguji, H, 1998, "An efficient CFD approach for simulating unsteady hypersonic shock-shock interference flows", *Computers and Fluids*, **27**, 571-580.

Zhou, J. G., Causon, D. M., Mingham C. G., and Ingram, D. M., 2001, "The surface gradient method for the treatment of source terms in the shallow-water equations", *J. Comp. Phys.*, **168**, 1-25.